An improved method for estimating the dissipation rate of turbulent kinetic energy using structure functions evaluated from the motion of finite-sized neutrally buoyant particles

Article

Accepted Version

An improved method for estimating the dissipation rate of turbulent kinetic energy using structure functions evaluated from the motion of finite-sized neutrally-buoyant particles

Miguel A. C. Teixeira[1, a)] and Catherine A. Mériaux[2]

[1)]*Department of Meteorology, University of Reading, Reading RG6 6ET, UK*

[2)]*ICTP-East African Institute for Fundamental Science, University of Rwanda, Kigali, Rwanda*

Statistical relations used for estimating the dissipation rate of turbulent kinetic energy (TKE) in isotropic turbulence from the inertial subrange of Lagrangian temporal and spatial structure functions are extended here to the case of more realistic turbulence spectra that include low frequency and low wavenumber ranges. It is shown that using the traditional relations based only on the inertial subrange substantially underestimates the dissipation. The improved relations are better constrained by experimental data from which the dissipation is evaluated, enabling more accurate dissipation estimates. The concept is illustrated using laboratory data from water tank experiments of turbulence generated by an oscillating cylinder, where the dissipation is evaluated in 3 independent ways: from Lagrangian spectra and from Lagrangian temporal and spatial structure functions calculated from the motion of neutrally-buoyant finite-sized particles. An additional correction to the relations for estimating the dissipation from the spatial structure functions is applied to take into account the filtering effect of the particles due to their finite size. It is found that, for these particular experiments, the TKE dissipation rate scales well with dimensionally consistent quantities built using the amplitude of the oscillation of the cylinder and the period of its motion, and the constant of proportionality in this scaling relation is determined using the method proposed here. Although the turbulence under consideration is quite anisotropic, the adopted theoretical framework, which assumes isotropic turbulence, seems to be applicable to the experimental data as long as the turbulence statistics are averaged over the 3 main flow directions.

I. INTRODUCTION

The dissipation rate of turbulent kinetic energy (TKE) (hereafter simply called dissipation) in turbulent flows is almost invariably estimated from measurements using results from Kolmogorov's theory, which postulates that the inertial subrange of the turbulence spectra is proportional to a power of the dissipation[1–3]. Conceptually, this procedure poses no problems when the dissipation is estimated directly from the spectra, but calculation of spectra from raw turbulence data always involves a certain amount of processing, with the underlying assumptions inevitably leading to some loss of accuracy. A more straightforward way to estimate the dissipation, at least from a data processing point of view, is by using the structure functions of the turbulence[4,5], for which Kolmogorov's results may be expressed equivalently as a proportionality of the structure functions to a power of the dissipation[6–8]. de Jong *et al.*[9] and Bertens *et al.*[10] give detailed accounts of how to estimate the dissipation from spectra and structure functions obtained in laboratory experiments using particle image velocimetry (PIV).

However, one aspect that is often overlooked is that Kolmogorov's theory only specifies the form of the turbulence spectrum in the inertial subrange, whereas the structure functions receive contributions from the whole spectrum[6]. This necessarily makes the relations that

are available to link the structure functions to the corresponding spectra inaccurate to some degree. Being based on the assumption that only the spectrum in the inertial subrange matters in this calculation, existing relations expressing the structure functions in terms of the dissipation are best suited to very large Reynolds number flows, where the inertial subrange extends over a wide range of scales. But this approach is subject to inaccuracies in real cases, where the inertial subrange may be narrow, or sampled at a resolution that is not fine enough. It is known that the inertial subrange displayed by structure functions is narrower than that displayed by the corresponding spectra (see figs. 1 and 2 of Ref. 11). Unlike what happens for quantities where the viscous cutoff of the spectra is of crucial importance, such as the direct calculation of the dissipation or of the acceleration variance from their definitions[12], in the evaluation of the dissipation from structure functions the low-wavenumber part of the spectrum plays a more important role.

Hence, in the present study the functional dependence of the Lagrangian temporal structure function and of the spatial structure functions on the dissipation in homogeneous and isotropic turbulence will be re-derived for energy spectra that include, not only an inertial subrange, but also a low wavenumber or low frequency range. These relations will then be applied to observational data coming from laboratory experiments by Mériaux *et al.*[5], (hereafter denoted as M2020) of turbulence generated in a water tank by an oscillating cylinder, moving in a Lissajous figure with an amplitude of 7.5 cm. In these

———
a)Corresponding author: m.a.teixeira@reading.ac.uk

experiments, turbulence statistics were diagnosed from the motion of neutrally-buoyant finite-sized particles immersed in the flow. Despite their relatively large size (diameter $D \approx 2\,\mathrm{cm}$ or $D/\eta = O(100 - 200)$, where η is the Kolmogorov microscale – see Table 2 of M2020), the particles were small enough to capture sufficient information on the inertial subrange of the turbulent motion. The reader is referred to M2020 for more details. Finite-sized particles immersed in a fluid have been used by numerous authors, either to study their clustering behaviour[13,14], the acceleration of the flow[15], or the rotation of the particles[16]. In this work, the particles are assumed to be purely passive and homogeneously distributed throughout the fluid, sampling the flow in an unbiased way.

The dissipation is evaluated here from the improved relations using the Lagrangian frequency spectrum of the turbulence, the Lagrangian temporal structure function and the spatial structure functions resulting from these experiments (the latter of which are evaluated using a methodology developed by Monaghan and Mériaux[17]). The results show that the dissipation estimates are all consistent, and correct a perceived underestimation of the dissipation, confirming the usefulness of the new relations.

This article is organized as follows. In section II, an overview is presented of the derivation of the statistical relations between the structure functions and the dissipation, and new extended relations are derived. In section III, spectra and structure functions are computed from laboratory data and fitted by their theoretical forms predicted by these new relations, yielding values of the dissipation. The dissipation is also shown to conform to a simple scaling, based on the physical characteristics of the experimental setup. Finally, section IV summarizes the main conclusions of this study.

II. METHODOLOGY

A. Established relations

An overview of the currently used approximations to relate turbulence spectra and structure functions (and thence estimate the dissipation) is necessary before the new, more refined appoximations, are introduced. It will be assumed in the theoretical treatment that the turbulence is statistically homogeneous, stationary and isotropic. Kolmogorov's hypothesis about the inertial subrange can be expressed for the wavenumber energy spectrum of the turbulence, $E(k)$, as

$$E(k) = \alpha \varepsilon^{2/3} k^{-5/3}, \tag{1}$$

where α is a constant (known as Kolmogorov's constant), ε is the dissipation and k is the wavenumber. For the Lagrangian frequency spectrum, $\phi(\omega)$, Kolmogorov's hy-

pothesis can be expressed as

$$\phi(\omega) = \beta \varepsilon \omega^{-2}, \tag{2}$$

where ω is the (angular) frequency and β is a coefficient (sometimes also known as Kolmogorov constant). Note, however, that β is actually a function of the Reynolds number of the flow[12,18]. The spectra presented above are defined such that

$$\frac{3}{2}\langle u_i^2 \rangle = \frac{3}{2}q^2 = \int_0^{+\infty} E(k)\,dk, \tag{3}$$

$$\langle u_i^2 \rangle = q^2 = \int_0^{+\infty} \phi(\omega)\,d\omega, \tag{4}$$

where the brackets denote ensemble averaging, u_i is a turbulent velocity component, and $i = 1, 2, 3$, correspond to the 3 spatial directions in a Cartesian coordinate system. q denotes the root-mean-square (RMS) turbulent velocity.

Relationships analogous to Eqs. (1) and (2) may be derived for both the spatial and the Lagrangian temporal structure functions. It seems fair to assume that the most fundamental relations are naturally formulated in spectral space, since arguments about the turbulence cascade are spectral by nature. The second-order Lagrangian temporal structure function is defined, in terms of the corresponding Lagrangian frequency spectrum, $\phi(\omega)$, as

$$D_T(\tau) = \langle [u_i(t + \tau) - u_i(t)]^2 \rangle$$
$$= 2\int_0^{+\infty} \phi(\omega)\,[1 - \cos(\omega\tau)]\,d\omega, \tag{5}$$

where t is an arbitrary time and τ is the time lag on which D_T depends. The second equality is equivalent to Eq. (13.31) of Monin and Yaglom[6]. For stationary turbulence, D_T does not depend on t, but only on τ. Using Eqs. (2) and (5), it can be shown that

$$D_T(\tau) = C_0 \varepsilon \tau, \tag{6}$$

and the coefficient C_0 satisfies $C_0 = \pi\beta$. Equation (6) is equivalent to Eq. (21.30') of Monin and Yaglom[6]. It should be noted that Eq. (6) is only valid for timescales within the inertial subrange of the Lagrangian frequency spectrum, for which Eq. (2) holds.

The relations expressing the spatial structure functions in terms of the wavenumber spectrum (to be presented next) are somewhat more involved. If the turbulence is assumed to be isotropic, any two perpendicular directions can be chosen for the velocity components and spatial lag l defining the longitudinal and transverse spatial structure functions. We choose these directions as x and y, respectively.

The longitudinal and transverse second-order spatial

structure functions, C_L and C_N, can then be defined as

$$C_L(l) = \langle [u_1(x+l, y, z) - u_1(x, y, z)]^2 \rangle$$

$$= 2 \iiint_{-\infty}^{+\infty} \Phi_{11}(\boldsymbol{k}) \left[1 - \cos(k_1 l)\right] dk_1 dk_2 dk_3, \quad (7)$$

$$C_N(l) = \langle [u_1(x, y+l, z) - u_1(x, y, z)]^2 \rangle$$

$$= 2 \iiint_{-\infty}^{+\infty} \Phi_{11}(\boldsymbol{k}) \left[1 - \cos(k_2 l)\right] dk_1 dk_2 dk_3, \quad (8)$$

where l is the space lag, Φ_{ij} (with $i, j = 1, 2, 3$) is the three-dimensional wavenumber spectrum of the turbulence and $\boldsymbol{k} = (k_1, k_2, k_3)$ is the wavenumber vector, which is related to k via $k = (k_1^2 + k_2^2 + k_3^2)^{1/2}$. Equations (7)-(8) are particular cases of Eq. (13.44) of Monin and Yaglom[6]. Since the turbulence is homogeneous, C_L and C_N do not depend on $\boldsymbol{x} = (x, y, z)$, but only on l.

In order to make progress in this calculation, it is necessary to introduce spherical polar coordinates for the wavenumber in the integrals of Eqs. (7)-(8), namely $k_1 = k \sin\theta \cos\varphi$, $k_2 = k \sin\theta \sin\varphi$ and $k_3 = k \cos\theta$, where θ and ϕ are angles. Then, using also the fact that, in isotropic turbulence we have[19]

$$\Phi_{ij}(\boldsymbol{k}) = \left(\delta_{ij} - \frac{k_i k_j}{k^2}\right) \frac{E(k)}{4\pi k^2} \quad (9)$$

(where δ_{ij} is the Kronecker delta), those equations become

$$C_L(l) = \frac{1}{2\pi} \int_0^{2\pi} \int_0^\pi \int_0^{+\infty} E(k) \sin\theta \left(\sin^2\theta \sin^2\varphi + \cos^2\theta\right)$$
$$\times \left[1 - \cos(kl \sin\theta \cos\varphi)\right] dk\, d\theta\, d\varphi, \quad (10)$$

$$C_N(l) = \frac{1}{2\pi} \int_0^{2\pi} \int_0^\pi \int_0^{+\infty} E(k) \sin\theta \left(\sin^2\theta \sin^2\varphi + \cos^2\theta\right)$$
$$\times \left[1 - \cos(kl \sin\theta \sin\varphi)\right] dk\, d\theta\, d\varphi. \quad (11)$$

If Eq. (1) is inserted into Eqs. (10)-(11), the change of variable $\rho = kl$ enables the dependences of C_L and C_N on l to be moved outside the integrals. Then the integrals can be simplified by reverting to Cartesian coordinates (but now with ρ taken as the radial coordinate), and adopting cylindrical coordinates to perform the integration. This enables an immediate integration along the azimuthal angle, and an analytical, although not so immediate, integration in the radial direction. The final result is

$$C_L(l) = C_k \left(\varepsilon l\right)^{2/3}, \quad C_N(l) = \frac{4}{3} C_k \left(\varepsilon l\right)^{2/3}, \quad (12)$$

where

$$C_k = \frac{36}{55} \alpha \int_0^{+\infty} \frac{1 - \cos x}{x^{5/3}} dx = \frac{54}{55} \alpha \int_0^{+\infty} \frac{\sin x}{x^{2/3}} dx. \quad (13)$$

Either integral in Eq. (13) needs to be evaluated numerically. The integral in the second equality of Eq. (13) can be evaluated to yield ≈ 1.34, which multiplied by $54/55$ and by $\alpha = 2$ (a value justified below) gives $C_k \approx 2.63$.

Equations (6) and (12) provide the classical results that we wish to improve.

B. Derivation of the extended relations

The extension of the wavenumber energy spectrum (Eq. (1)) that includes a low-wavenumber range is known as a Von Kármán spectrum[20], and can be expressed as the model spectrum

$$E(k) = \frac{\alpha \varepsilon^{2/3} L^{5/3} (kL)^4}{[C + (kL)^2]^{17/6}}, \quad (14)$$

where C is an adjustable dimensionless constant and L is the longitudinal integral length scale of the turbulence, defined as

$$L = \frac{\pi}{2q^2} \int_0^{+\infty} k^{-1} E(k) dk. \quad (15)$$

The constants α and C can be determined theoretically by requiring that $E(k)$, as given by Eq. (14), satisfy both Eqs. (3) and (15). This yields

$$C = \left(\frac{27\pi}{110}\right)^2 \left(\int_0^{\pi/2} \sin^4\theta \sec^{1/3}\theta\, d\theta\right)^{-2} \approx 0.5578 \quad (16)$$

(where the integral needs to be evaluated numerically) and

$$\alpha = \frac{55}{9\pi} C^{5/6} \left(\frac{\varepsilon L}{q^3}\right)^{-2/3}. \quad (17)$$

Since the Von Kármán spectrum (Eq. (14)) is valid at infinite Reynolds number, $\varepsilon L / q^3$ in Eq. (17) should be taken also in the infinite Reynolds number limit. It is known from DNS and experiments that $\varepsilon L / q^3 \approx 0.5$ in that limit (see, e.g. fig. 2 of Teixeira and Mériaux[12] or Refs. 8 and 21). Choosing, for example, $\varepsilon L / q^3 = 0.46$, Eq. (17) yields $\alpha = 2$, as was seen previously to be appropriate to assume for a Von Kármán spectrum[12,19,20]. This value will be adopted here.

The extension of the Lagrangian frequency spectrum (Eq. (2)) to low frequencies is sometimes called a Lorenz spectrum[11,12,22], and can be expressed as the model spectrum

$$\phi(\omega) = \frac{\beta \varepsilon}{\omega_0^2 + \omega^2}, \quad (18)$$

where ω_0 is an adjustable coefficient, which is related to the integral time scale T_L,

$$T_L = \frac{1}{q^2} \int_0^{+\infty} \langle u_i(t) u_i(t+\tau) \rangle d\tau$$
$$= \frac{\pi}{2q^2} \phi(\omega = 0) = \frac{\pi}{2q^2} \frac{\beta \varepsilon}{\omega_0^2}. \quad (19)$$

From Eqs. (4) and (18), it also follows that

$$\langle u_i^2 \rangle = q^2 = \frac{\pi}{2} \frac{\beta \varepsilon}{\omega_0}. \tag{20}$$

Eqs. (19) and (20) imply, more simply, that $\omega_0 = 1/T_L$, as noted by Mordant et al.[22]

If the same procedure used to obtain the second-order Lagrangian temporal structure function (Eq. (6)) is followed, but using $\phi(\omega)$ defined according to Eq. (18) in Eq. (5), this yields

$$D_T(\tau) = C_0 \varepsilon \tau \frac{1 - e^{-\omega_0 \tau}}{\omega_0 \tau} = \frac{C_0 \varepsilon}{\omega_0} \left(1 - e^{-\omega_0 \tau} \right). \tag{21}$$

Note that, unlike Eq. (6), in which D_T grows linearly with τ, D_T as given by Eq. (21) approaches a constant at large τ, namely

$$D_T(\tau \to +\infty) = \frac{C_0 \varepsilon}{\omega_0}. \tag{22}$$

Note also that in the limit $\omega_0 \tau \to 0$, i.e. for time lags τ contained in the inertial subrange, which are relatively short compared with $1/\omega_0$, Eq. (21) reduces to Eq. (6).

As for D_T, the procedure used in section II-A to derive the second-order longitudinal and transverse spatial structure functions (Eq. (12)) can be extended by considering the wavenumber spectrum $E(k)$ of Eq. (14) instead in Eqs. (10)-(11). After substantial calculations, where the changes of variables of integration follow much the same procedure as described previously, the following results are obtained:

$$C_L(l) = \frac{36}{55} \alpha \left(\varepsilon l \right)^{2/3} \left(\frac{L}{l} \right)^{5/3} \int_0^{+\infty} \frac{1 - \cos x}{\left[C + \left(\frac{L}{l} \right)^2 x^2 \right]^{5/6}} dx, \tag{23}$$

$$C_N(l) = \frac{6}{55} \alpha \left(\varepsilon l \right)^{2/3} \left(\frac{L}{l} \right)^{5/3}$$
$$\times \int_0^{+\infty} \frac{3C + 8 \left(\frac{L}{l} \right)^2 x^2}{\left[C + \left(\frac{L}{l} \right)^2 x^2 \right]^{11/6}} \left(1 - \cos x \right) dx. \tag{24}$$

Unfortunately, C_L and C_N cannot be formulated now as compactly as in Eq. (12), because their dependence on l extends into the integrals, which cannot be evaluated analytically. However, it can be shown that in the limit $l/L \to 0$, Eqs. (23)-(24) reduce to Eq. (12), as they should. This is the limit of relatively small scales, which are those contained in the inertial subrange of the wavenumber spectrum. Conversely, and although this is not as clear, C_L and C_N both approach constants in the opposite limit, i.e. as $l/L \to \infty$.

1. Correction for particle filtering

To make a comparison of the spatial structure functions with data easier, it must be taken into account that the finite-sized particles used to probe the turbulent flow are unable to resolve spatial scales smaller than their own size. Following Teixeira and Mériaux[12], this is taken into account here by multiplying the structure functions given by Eqs. (23)-(24) by the following factor

$$\left(\frac{l}{\pi D} \right)^2 \sin^2 \left(\frac{\pi D}{l} \right) \tag{25}$$

(valid for $D/l \leq 1$, and zero otherwise), where D is the particle diameter. Equation (25) was obtained directly from Eq. (24) of Ref. 12 (equivalent to Eqs. (5.6) and (5.7) of Ref. 3, where this approach was introduced), by replacing $k = 2\pi/l$, noting that a spatial displacement l corresponds to a wavenumber $2\pi/l$. This approach takes into account the fact that when particles are at a distance D from each other, they are in contact, therefore C_L or C_N should both be zero: the multiplicative correction of Eq. (25) approaches 1 when $D/l \to 0$, but becomes 0 at $D/l = 1$ (or higher), which makes sense physically.

Although this filtering certainly has an impact in the frequency/temporal domain, that impact is more uncertain, as a translation of spatial filtering into the temporal domain presupposes a 'dispersion relation' for the turbulence. While such a relationship between spatial and temporal scales certainly exists in a fuzzy sense[3,23], it cannot be quantified precisely, as in turbulence all scales interact with each other and, for example, high wavenumbers k in $E(k)$ may correspond to both low and high frequencies ω in $\phi(\omega)$.

III. RESULTS

A. Testing of the new relations

Equations (18), (21) and (23)-(24) will be used next to independently estimate the dissipation from the data of laboratory experiments described by M2020, in which Lagrangian spectra, temporal structure functions and spatial (originally, only longitudinal) structure functions were evaluated from the motion of finite-sized neutrally-buoyant particles. The turbulence produced by the oscillating cylinder in these experiments was naturally anisotropic (unlike, for example, in Ref. 24), nevertheless the theoretical relations presented above will be applied to the data by averaging the spectra and structure functions over the 3 spatial directions. The hope is that the isotropic theory will still hold in anisotropic conditions.

Figure 1 shows the compensated Lagrangian frequency spectra, Lagrangian temporal structure functions, spatial longitudinal structure functions and spatial transverse structure functions calculated from both experiments 4, 6, 7, 8, 10 and 11 of M2020 (see their Tables 1 and 2), and Eqs. (18), (21) and (23)-(24). We note that all these compensated quantities are such that the inertial subrange corresponds to a horizontal line, whose height indicates the value of ε.
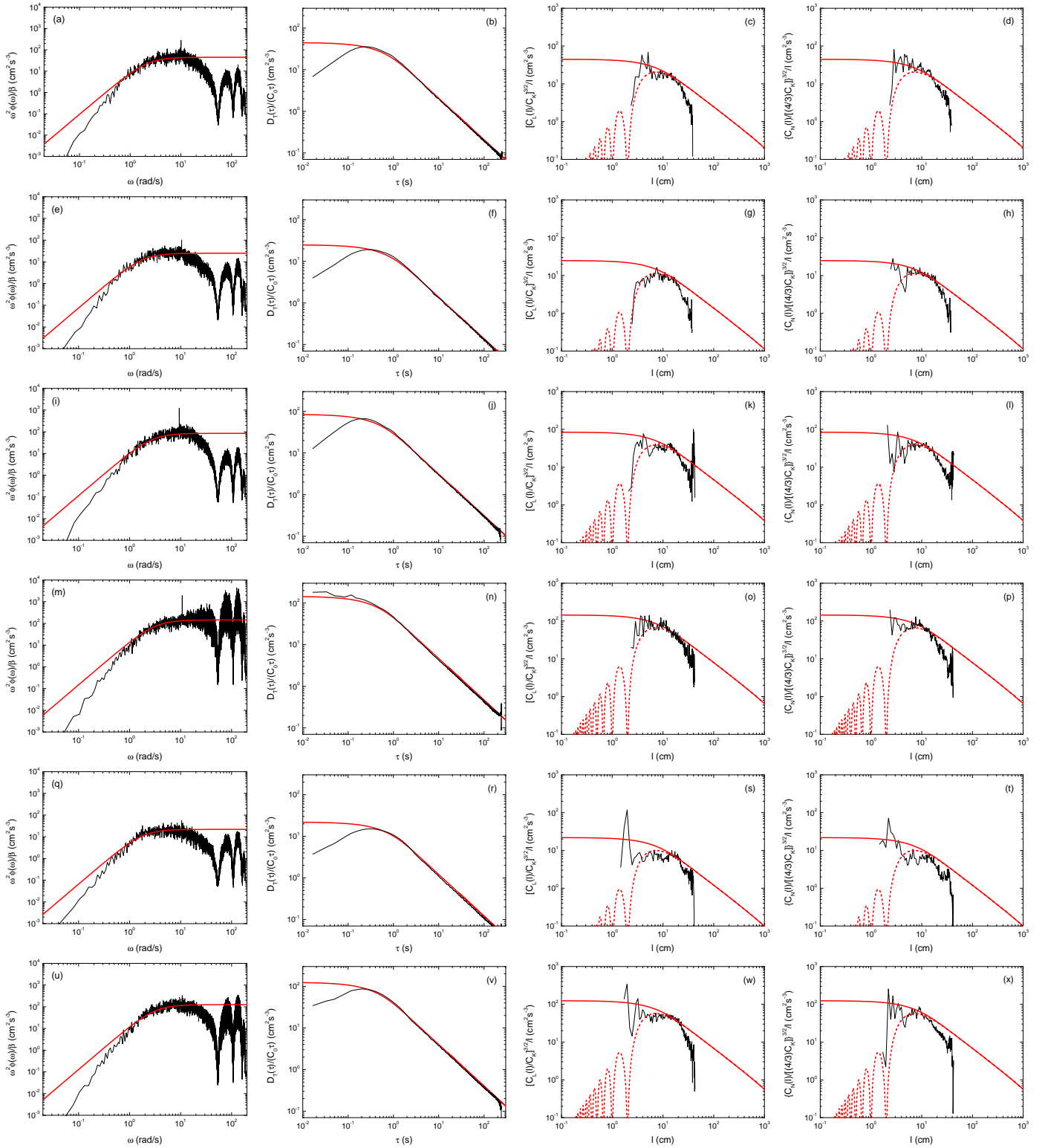
FIG. 1. Compensated Lagrangian frequency spectra $\omega^2 \phi(\omega)/\beta$ as a function of ω for experiments 4, 6, 7, 8, 10 and 11 of M2020 in respectively (a),(e),(i),(m),(q),(u). Compensated second-order Lagrangian temporal structure function $D_T(\tau)/(C_0\tau)$ as a function of τ for experiments 4, 6, 7, 8, 10 and 11 of M2020 in respectively (b),(f),(j),(n),(r),(v). Compensated second-order longitudinal spatial structure function $[C_L(l)/C_k]^{3/2}/l$ as a function of l for experiments 4, 6, 7, 8, 10 and 11 of M2020 in respectively (c),(g),(k),(o),(s),(w). Compensated second-order transverse spatial structure function $\{C_N(l)/[(4/3)C_k]\}^{3/2}/l$ as a function of l for experiments 4, 6, 7, 8, 10 and 11 of M2020 in respectively (d),(h),(l),(p),(t),(x). Black lines denote experimental data averaged over the 3 spatial directions; solid red lines correspond to the fits provided by Eqs. (18), (21), (23) and (24), respectively; dashed red lines correspond to Eqs. (23) and (24) multiplied by Eq. (25) (where the portion to the left of $l = D = 2$ cm should be ignored).

The Lagrangian frequency spectrum is presented as $\omega^2\phi(\omega)/\beta$ as a function of ω, assuming that $C_0 = 5$, or equivalently $\beta = 1.6$. Although β actually depends on the Reynolds number of the flow, as pointed out by Teixeira and Mériaux[12], the range of Reynolds numbers considered in the selected experiments of M2020 is limited enough ($Re_\lambda \approx 306 - 418$) that this value is reasonable (see, for example, fig. 3 of Ref. 12). There is another adjustable parameter in the Lagrangian frequency spectrum: ω_0. It would in principle be possible to estimate this parameter independently from the experimental data by calculating the integral time scale T_L using Eq. (19), or an equivalent expression based on the temporal structure function, namely

$$T_L = \frac{1}{2q^2} \int_0^{+\infty} [D_T(\tau \rightarrow +\infty) - D_T(\tau)]\, d\tau, \qquad (26)$$

which results from Eqs. (5) and (19). However, T_L calculated in this way converges poorly, perhaps because of insufficient sampling, or the limited extent of the tank used in the experiments. Although tentative estimates of T_L using this method suggest that it takes values of the same order as those that are going to be obtained next, it is more reliable to estimate ω_0 by trial and error from the values that optimize the fit of the theoretical prediction (Eq. (18)) to the experimental data. In order to avoid the weak constraint that this procedure, by itself, would place on ω_0, it was decided to assume additionally that ω_0 scales inversely with the period T of the oscillation of the cylinder. It was found that the relation

$$\omega_0 = \frac{1}{T_L} = \frac{5.462}{T} \qquad (27)$$

best describes this dependence, so it will be adopted hereafter.

The temporal structure function is plotted in fig. 1 as $D_T(\tau)/(C_0\tau)$ as a function of τ, which means that according to Eq. (21) it also depends on ω_0 (assuming the same value of C_0 as for the Lagrangian frequency spectrum). For consistency, here ω_0 is also calculated according to Eq. (27).

Finally, the spatial longitudinal and transverse structure functions are plotted in fig. 1 as $[C_L(l)/C_k]^{3/2}/l$ and $\{C_N(l)/[(4/3)C_k]\}^{3/2}/l$, respectively, as a function of l. For $\alpha = 2$, as assumed previously, these quantities depend, according to Eqs. (23)-(24), on the longitudinal integral length scale of the turbulence L. As the integral time scale, the longitudinal integral length scale could also, in principle, be calculated independently from the data using its definition, Eq. (15), or its equivalent in terms of a spatial structure function. However, due to poor convergence of the calculation, in this case resulting directly from the limited extent of the tank, it is better to treat it as an adjustable parameter. The relevant basic parameter of the experiments that has dimensions of length is the amplitude of the cylinder motion $A = 7.5$ cm. So L should be proportional to this quantity.

TABLE I. Parameters of the Experiments and theoretical fits shown in fig. 1: the period of the cylinder motion T, the RMS velocity q, the longitudinal integral length scale L, ω_0, and the dissipation ε. Values of T and q come from Tables 1 and 2 of M2020, respectively. Note that q results from the average of the velocity variances of the 3 velocity components.

Experiment	T(s)	$q(\mathrm{cm\,s^{-1}})$	L(cm)	$\omega_0(\mathrm{rad\,s^{-1}})$	$\varepsilon(\mathrm{cm^2\,s^{-3}})$
4	2.5	7.0	4	2.185	45
6	3	5.7	4	1.821	25
7	2	8.6	4	2.731	85
8	1.75	10.3	4	3.121	145
10	3	5.2	4	1.821	22
11	1.75	9.6	4	3.121	125

Since A does not change throughout the experiments, here a constant value of the longitudinal integral length scale will be assumed, which optimizes agreement with the data: $L = 4$ cm, i.e. $L = 0.533A$. Note that this value of the longitudinal integral length scale is smaller than the values of M2020 in their Table 2, because the integral length scale in M2020 was simply defined as $L = q^3/\varepsilon$ (cf. Ref. 25), whereas it can be shown that L, as defined by Eq. (15), obeys instead $L = C_\varepsilon q^3/\varepsilon$, where C_ε is a constant lower than 1, as pointed out previously[12]. Interestingly, the value of L found in the present study is consistent with the length scale found for the transition between the ballistic and diffusive dispersion regimes in figs. 11 and 13 of M2020.

Table I shows all the relevant parameters for the experiments that were used to estimate the dissipation in fig. 1, namely the number of the experiment, the period of the cylinder motion T, the RMS velocity q (as given in Table 2 of M2020), the assumed longitudinal integral length scale L, ω_0 derived from T according to Eq. (27), and the dissipation ε estimated (by trial and error) from the optimal fit of the red lines to the black lines in the graphs of fig. 1. Using the values of L and ω_0 given in Table I, the values for ε obtained from the best fits (red lines in fig. 1) are found to be identical across the turbulence statistics for each experiment, showing the consistency of the proposed method.

The fits of the Lagrangian frequency spectra in fig. 1 are fairly good. Although the regions that separate the inertial subrange from the low-frequency range appear to be well-captured, the measured spectra depart from the fits both at low and at high frequencies. Note that only the horizontal portion of the theoretical prediction would exist if only the inertial subrange was taken into account, as is traditionally done. At high frequencies, the departure of the measured spectra from the theoretical prediction is caused by the aliasing associated with the finite dimensions of the particles used to probe the turbulence. This is shown by the oscillations visible in the black lines at the highest frequencies. These oscillations might be viewed as a manifestation of the spatial ex-

tent of the particles, related to a corresponding temporal extent through the fuzzy 'dispersion relation' that represents the spatio-temporal structure of the turbulence[11]. Curiously, the spectrum has more energy at high frequencies in Experiment 8, and to a lesser extent in Experiment 11, for reasons which are not obvious. At low frequencies, the spectra evaluated from measurements also have less energy than their fits. This may be either an effect of the spatial confinement of the turbulence (which temporally translates into a deficit of energy at low frequencies), or may be an effect of the way in which the spectra are obtained from the raw data by Fourier transformation. It is worth mentioning that the approach used to calculate the spectra as proportional to the square of the Fourier transform of the original temporal signal is strictly accurate for time series of infinite extent, being subject to errors for finite time series.

The measured temporal structure functions in fig. 1 are quite smooth, perhaps as a result of being less processed that the frequency spectra. The theoretical fits to these functions are quite satisfactory to the right of their maxima, but the experimental data fall below the theoretical fits to the left of these maxima, except for Experiment 8, for reasons which are not obvious. It can be noticed that the inertial subrange in the temporal structure functions is almost non-existent in most cases. This is consistent with figs. 1 and 2 of Lien and D'Asaro[11], which show that a well defined inertial subrange exists in the structure function only at substantially higher Reynolds numbers than it does for the spectrum. The overestimation of the experimental data by the fits to the left of the maxima is obviously due to the aliasing introduced by the finite dimensions of the particles used to probe the turbulence, being a counterpart of the phenomenon observed for the spectra at high frequencies. However, no disagreement is observed between experimental data and the fits for high values of τ, which is surprising, given the disagreement of the spectra at low frequencies. This suggests that perhaps the temporal structure function at high τ is weakly sensitive to the form of the spectrum at low frequencies. In any case, the prediction that $D_T(\tau)$ approaches a constant at high τ is clearly confirmed by the data. Note that, using the traditional formula for $D_T(\tau)$, $D_T(\tau)/(C_0\tau)$ is predicted to be constant, corresponding to the low τ asymptote of the theoretical predictions (red lines). If this classical theoretical prediction (horizontal red line) was fitted to the brief plateau exhibited by the experimental data and corresponding to the maximum values of $D_T(\tau)/(C_0\tau)$ (the inertial subrange), this fit would be, on the one hand, rather uncertain, since this plateau has a very limited extent. On the other hand, the value of ε estimated from this fit would underestimate the dissipation by up to a factor of 2, since it would be substantially lower than the asymptote of the new theoretical prediction at low τ (red line). An underestimation of ε relative to the values contained in Table I is, indeed, seen in Table 2 of M2020, whose estimates were based on the fit of a horizontal line to the short plateau shown by $D_T(\tau)/(C_0\tau)$ in fig. 1. It should also be stressed that the fit of $D_T(\tau)$ for high values of τ, which the present method is able to provide, is considerably more reliable than any fit at lower τ, since it refers to large timescales, presumably corresponding to large length scales, which are well resolved by the probing particles. For all these reasons, the improved formula for $D_T(\tau)$, Eq. (21), is crucial to achieve consistency between ε obtained from the frequency spectrum and the temporal structure function.

The measured spatial structure functions in fig. 1 are somewhat noisier than the temporal structure functions, which may be a consequence of the smaller sample used to calculate them (see details in M2020). The experimental data (black lines) are now compared directly with the theoretical predictions of Eqs. (23) and (24) (solid red lines), and with the same theoretical predictions corrected for the finite size of the probing particles (dashed red lines). The traditional relations for the compensated spatial structure functions would correspond to a constant (horizontal lines) that, if fitted to the experimental data (plateaus in the black lines), would again produce considerably lower estimates of ε than the ones obtained using the improved relations. At low values of l, the theoretical predictions (solid red lines) depart from the measured structure functions, due to the finite size of the probing particles. This is partly captured by the theoretical predictions corrected for particle size filtering (dashed lines), however, there are some discrepancies. For example, the extension of non-zero values of the structure functions for $l < 2$ cm, i.e. for separations smaller than the diameter of the particles $D = 2$ cm in fig. 1, might be caused by measurement errors. At high values of l, the structure functions calculated from measurements are limited by the dimensions of the domain where the experiments are performed, which are 30 cm in all directions. This causes not only the sudden cutoff of the experimental data (see right end of the black lines), but also their decay at high l at a rate faster than predicted theoretically (red lines). Whereas the exact limits of the frequency spectrum and temporal structure function are rather fuzzy, because the turbulence does not satisfy a 'dispersion relation', the limits of the domain of the spatial structure function are rigidly defined by the size of the probing particles and of the tank. The spike near the upper limit of l in Experiment 7 is not easy to interpret, but overall the corrected theoretical predictions (dashed red lines) seem to be in reasonable agreement with the experimental data (black lines), corroborating the values of ε estimated from the frequency spectra and temporal structure functions.

All these results illustrate the advantages of the improved relations of the temporal and spatial structure functions for estimating ε reliably. In the following section, it will be analysed to what extent the basic parameters of the experiments can be used to scale the RMS velocity and dissipation in this turbulent flow.

B. Scaling of the turbulence characteristics

Apart from the size of the tank in which the experiments of M2020 were performed, the obvious length and time scales that the experimental setup contains are the amplitude of the motion of the cylinder that generates the turbulence A and the period of its oscillations T. We would expect the characteristics of the turbulence to be scaled by these quantities. This idea is tested next.

Figure 2 shows comparisons between various scalings using A and T, for the RMS velocity q and for the dissipation ε, compared with the measurements of q made by M2020 and with the values of ε estimated using the method developed in the present study. fig. 2(a) shows that the RMS velocity scales fairly well with A/T, approximately following the relation

$$q = 1.15\frac{2A}{T} = 0.79\frac{L}{T_L}. \tag{28}$$

There is a slight departure from this scaling between Experiments 6 and 10, and between Experiments 8 and 11, for which the scaling would predict the same RMS velocity (given that both A and T are equal for these pairs of experiments), but q is larger for Experiments 6 and 8. This is because the RMS velocity depends (albeit weakly) on the direction of initial motion of the cylinder, with q being slightly lower when the initial motion is upward, an aspect noted by M2020. In M2020, T_L ranges, among the experiments selected in the present study, from 0.6 s in Experiment 8 to 1.4 s in Experiment 10, roughly following a proportionality to T, as hypothesized here (Eq. (27)). Our values of T_L range instead from 0.32 s in Experiments 8 and 11 to 0.55 s in Experiments 6 and 10. This means that the present values are smaller by a factor of 0.4-0.5. Such a difference can be explained by the way T_L was simply estimated in M2020 from the point where the velocity correlation function changes sign instead of calculating the integral in the first equality of Eq. (19). The velocity correlation function in fig. 10b of M2020 decreases approximately exponentially, but crossing zero (cf. fig. 1 of Ref. 22). If this variation is approximated as linear, it can be shown that the integral of such a correlation function is less than the value of the time lag when the function reaches zero, by a factor 0.5. The concave upward curvature of the measured correlation function means that this value is probably a slight overestimate. Now, the second equality of Eq. (28) shows that q can also be expressed in terms of L and T_L (using $L = 0.533A$ and Eq. (27)), which is equivalent to $T_L = 0.79L/q$. In M2020, T_L was found to be $T_L = 0.6L/q$. The constants of proportionality in Eq. (28) and M2020 are therefore roughly similar, and consistent with the fact that both our L and T_L are half the values estimated by M2020.

Figure 2(b) presents a scaling for the dissipation based on A and T compared with the values of ε estimated before in Table I. This scaling is expressed by the relation

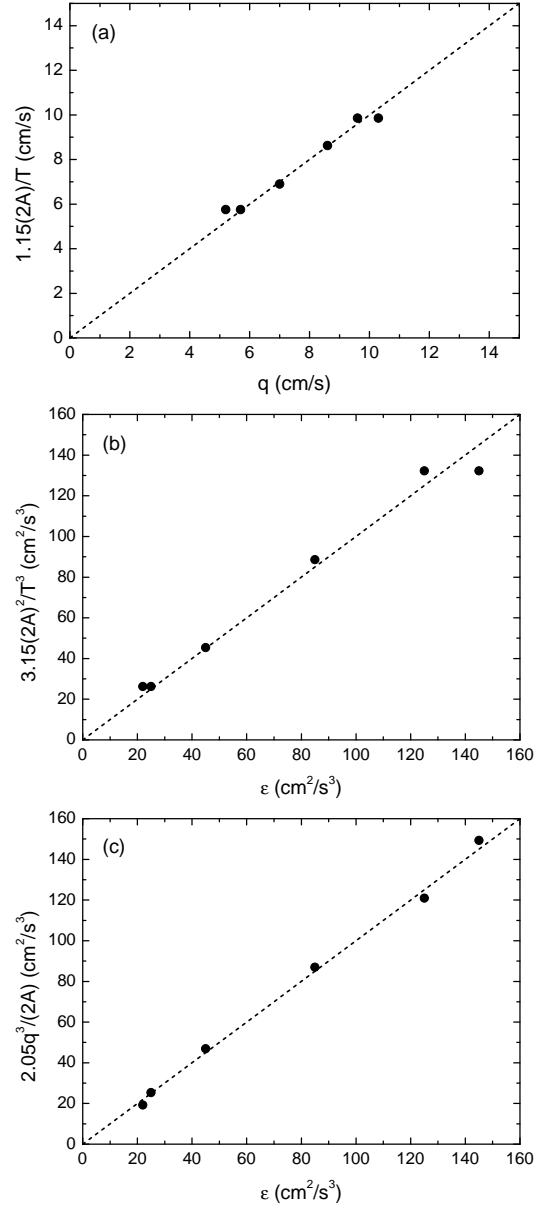$$\varepsilon = 3.15\frac{(2A)^2}{T^3} = 0.27\frac{L^2}{T_L^3}, \tag{29}$$

FIG. 2. (a) RMS velocity scaled using A and T vs the RMS velocity measured by M2020 (given in Table I); (b) dissipation scaled using A and T vs the dissipation estimated from the procedure developed in the present study; (c) dissipation scaled using the RMS velocity and A vs the dissipation estimated from the procedure developed in the present study. Symbols correspond to different experiments, and the dashed lines correspond to the predictions of Eqs. (28)-(30).

which can also be expressed in terms of L and T_L by the second equality. The dissipation obeys this scaling fairly well, except for its two highest values, corresponding to Experiments 8 and 11, where the scaling does not predict any difference in ε, but the values estimated from the spectra and structure functions are different. This is a consequence of the same phenomenon mentioned above for the RMS velocity, amplified, for the highest value of

Accepted to Phys. Fluids 10.1063/5.0148473

9

ε, by the fact that T appears in the scaling expression of Eq. (29) raised to the power of 3, instead of 1.

Finally, fig. 2(c) shows a scaling relation where the measured q is included, in combination with A, in the form

$$\varepsilon = 2.05 \frac{q^3}{2A} = 0.546 \frac{q^3}{L}, \tag{30}$$

(with the second equality using again the relation $L = 0.533A$), and this is compared with the ε estimated from the spectra and structure functions. As may be seen, this scaling is even more accurate than the one in fig. 2(b), corroborating the idea that not accounting for the effects of the direction of the initial motion of the cylinder is what causes the slight disagreement with the scaling of Eq. (29), manifested through its dependence on T. The accuracy of Eq. (30), still keeping A as a (constant) scaling parameter, is very good, as clearly shown by fig. 2(c). It is worth noting that if the definitions of q provided by Eq. (28) are inserted into Eq. (30), the scaling constants that appear in equations similar Eq. (29) are 3.12 and 0.27, respectively, which (unsurprisingly) are quite close to 3.15 and 0.27. This indicates that L and T_L have been correctly related to the physical properties of the experimental setup. It is also interesting that the constant included in the second equality of Eq. (30) (0.546) is slightly larger, but relatively close, to the value of $\varepsilon L/q^3$ previously assumed in Eq. (17) at infinite Reynolds number (0.46). The discrepancy goes in the right direction and the value is of the correct order of magnitude for a flow at the Reynolds numbers used in the experiments (see fig. 2 of Teixeira and Mériaux[12]).

These results show that the characteristics of the turbulence generated in the experiments of M2020 can be scaled with the key parameters of the experimental setup, which is not surprising. However, it would have been impossible to determine the exact form of these relationships, namely the corresponding proportionality constants, without fitting a theoretical model to the measurements. In the case of ε, this is much facilitated by the new statistical relations proposed in the present study.

IV. CONCLUSIONS

Statistical relations that have been traditionally used to estimate the dissipation rate of TKE from the spectra and structure functions in a turbulent flow have a validity that is limited to scales within the inertial subrange. In this study, new relations were derived for the temporal and spatial structure functions in isotropic turbulence, which result from formal definitions of these quantities where the energy spectra of the turbulence also include a low-wavenumber or low-frequency range. This was done by assuming a Von Kármán wavenumber spectrum and a Lorenz Lagrangian frequency spectrum. The resulting improved definitions of the structure functions are better suited to obtaining consistent and reliable estimates of the dissipation from these different flow statistics, particularly when they are evaluated from the motion of finite-sized neutrally-buoyant particles.

Data from the laboratory experiments of M2020 were used to test the new relations. It was seen that, despite the need to adjust additional parameters, namely ω_0 and L, these relations allowed the values of ε to be better constrained by the spectra and structure functions calculated from the experimental data than the classic relations. As the inertial subrange diagnosed from the particle motion is somewhat narrow, partly because the Reynolds number of the flow is not very high, but primarily because of the aliasing of small scales inherent to the finite size of the particles, spectra that have a low-wavenumber or low-frequency range add precious information to the structure functions. This is particularly clear in the case of the Lagrangian temporal structure function, where the existence of the high-τ asymptotic behaviour (corresponding to the low-frequency range of the Lagrangian spectra) is confirmed by the data, and greatly facilitates fitting the theory to the data in fig. 1.

Good fits of the frequency spectra, temporal structure functions and spatial structure functions predicted theoretically to the data were seen to correspond to consistent values of the dissipation from all these statistics for each experiment of M2020. The estimated values of ε are somewhat larger (by factors between 1.3 and 1.9) than those originally determined by M2020, suggesting an underestimation of the latter, as expected for situations in which the inertial subrange is narrow. Although the theoretical framework that was used and improved here is, in principle, only valid for isotropic turbulence, it was seen to be applicable to the considerably anisotropic turbulence generated in the laboratory experiments of M2020, if the turbulence statistics are averaged over the 3 spatial directions.

It was also shown that the characteristics of the turbulence (RMS velocity and dissipation) scale on the physical characteristics of the experimental setup associated with the stirring, namely the amplitude of the oscillating motion of the cylinder and the period of this oscillation. Knowing these scalings is, however, insufficient to evaluate q and ε, as the proportionality constants included in the scaling relations can only be obtained after estimating those quantities independently, by fitting the measurements to a model, as is done here. As these scalings are expressed in terms of quantities specific to the experimental setup adopted by M2020, their generality is probably limited. The equivalent scalings expressed in terms of the integral length and time scales, however, are likely to be more general.

All of the dissipation estimates in this paper have relied on an evaluation (and modelling) of second-order flow statistics. It would also be interesting to estimate the dissipation from the third-order spatial structure function, for which an exact theoretical result exists in the inertial subrange (Kolmogorov's 4/5 law) (see Eq. (6) of Ref. 8). Although this is beyond the scope of the present

study, it is an interesting idea for future work.

DATA AVAILABILITY

The data that support the findings of this study are available from the corresponding author upon reasonable request.

REFERENCES

[1]E. A. Terray, M. A. Donelan, Y. C. Agrawal, W. M. Drennan, K. K. Kahma, A. J. W. III, P. A. Hwang, and S. A. Kitaigorodskii, "Estimates of kinetic energy dissipation under breaking waves," J. Phys. Oceanogr. **26**, 792–807 (1996).

[2]W. M. Drennan, M. A. Donelan, E. A. Terray, and K. B. Katsaros, "Oceanic turbulence dissipation measurements in swade," J. Phys. Oceanogr. **26**, 808–815 (1996).

[3]R.-C. Lien, E. A. D'Asaro, and G. T. Dairiki, "Lagrangian frequency spectra of vertical velocity and vorticity in high-reynolds-number oceanic turbulence," J. Fluid Mech. **362**, 177–198 (1998).

[4]A. Jabbari, A. Rouhi, and L. Boegman, "Evaluation of the structure function method to compute turbulent dissipation within boundary layers using numerical simulations," J. Geophys. Res. Oceans **121**, 5888–5897 (2016).

[5]C. A. Mériaux, M. A. C. Teixeira, J. J. Monaghan, R. Cohen, and P. Cleary, "Dispersion of finite-size particles probing inhomogeneous and anisotropic turbulence," Eur. J. Mech. B - Fluids **84**, 93–109 (2020).

[6]A. S. Monin and A. M. Yaglom, Statistical Fluid Mechanics: Mechanics of Turbulence, volume 2 (MIT Press, 1981).

[7]P. K. Yeung, "Lagrangian investigations of turbulence," Ann. Rev. Fluid Mech. **34**, 115–142 (2002).

[8]T. Ishihara, T. Gotoh, and Y. Kaneda, "Study of high-reynolds number isotropic turbulence by direct numerical simulation," Ann. Rev. Fluid Mech. **41**, 165–180 (2009).

[9]J. de Jong, L. Cao, S. H. Woodward, J. P. L. C. Salazar, L. R. Collins, and H. Meng, "Dissipation rate estimation from piv in zero-mean isotropic turbulence," Exp. Fluids **46**, 499–515 (2009).

[10]G. Bertens, D. V. der Voort, H. Bocanegra-Evans, and W. van de Water, "Large-eddy estimate of the turbulent dissipation rate using piv," Exp. Fluids **56**, 89 (2015).

[11]R.-C. Lien and E. A. D'Asaro, "The kolmogorov constant for the lagrangian velocity spectrum and structure function," Phys. Fluids **14**, 4456–4459 (2002).

[12]M. A. C. Teixeira and C. A. Mériaux, "Estimating the filtering of turbulence properties by finite-sized particles using analytical energy spectra," Phys. Fluids **34**, 045117 (2022).

[13]L. Fiabane, R. Volk, J.-F. Pinton, R. Monchaux, A. Cartellier, and M. Bourgoin, "Do finite-size buoyant particles cluster?" Phys. Scr. , 014056 (2013).

[14]N. Machicoane, R. Zimmermann, L. Fiabane, M. Bourgoin, J.-F. Pinton, and R. Volk, "Large sphere motion in a nonhomogeneous turbulent flow," New J. Phys. **16**, 013053 (2014).

[15]E. Calzavarini, R. Volk, M. Bourgoin, E. Lévêque, J.-F. Pinton, and F. Toschi, "Acceleration statistics of finite-sized particles in turbulent flow: the role of faxén forces," J. Fluid Mech. **630**, 179–189 (2009).

[16]N. Pujara and E. A. Variano, "Rotations of small, inertialess, triaxial ellipsoids in isotropic turbulence," J. Fluid Mech. **821**, 517–538 (2017).

[17]J. J. Monaghan and C. A. Mériaux, "What can we learn from large bodies moving in a turbulent fluid," Eur. J. Mech. B. - Fluids **72**, 519–530 (2018).

[18]M. Barjona and C. B. da Silva, "Kolmogorov's lagrangian similarity law revisited," Phys. Fluids **29**, 105106 (2017).

[19]M. A. C. Teixeira and S. E. Belcher, "Dissipation of shear-free turbulence near boundaries," J. Fluid Mech. **422**, 167–191 (2000).

[20]S. B. Pope, Turbulent Flows (Cambridge University Press, 2000).

[21]L. Djendi, N. Lefeuvre, M. Kamruzzaman, and R. A. Antonia, "On the normalized dissipation parameter c_ϵ is decaying turbulence," J. Fluid Mech. **817**, 61–79 (2017).

[22]N. Mordant, P. Melz, O. Michel, and J.-F. Pinton, "Measurement of lagrangian velocity in fully-developed turbulence," Phys. Rev. Lett. **21**, 214501 (2001).

[23]J. C. H. Fung, J. C. R. Hunt, N. A. Malik, and R. J. Perkins, "Kinematic simulation of homogeneous turbulence by unsteady random fourier modes," J. Fluid Mech. **236**, 281–318 (1992).

[24]G. Bellani and E. A. Variano, "Homogeneity and isotropy in a laboratory turbulent flow," Exp. Fluids **55**, 1646 (2014).

[25]N. Mordant, E. Lévêque, and J.-F. Pinton, "Experimental and numerical study of the lagrangian dynamics of high reynolds turbulence," New J. Phys. **6**, 116 (2004).